



HAL
open science

Zero-Order Second Harmonic Generation from AlGaAs-on-Insulator Metasurfaces

Giuseppe Marino, Carlo Gigli, Davide Rocco, Aristide Lemaître, Ivan Favero,
Costantino de Angelis, Giuseppe Leo

► **To cite this version:**

Giuseppe Marino, Carlo Gigli, Davide Rocco, Aristide Lemaître, Ivan Favero, et al.. Zero-Order Second Harmonic Generation from AlGaAs-on-Insulator Metasurfaces. ACS photonics, 2019, 6 (5), pp.1226-1231. 10.1021/acsp Photonics.9b00110 . hal-03453409v2

HAL Id: hal-03453409

<https://hal.science/hal-03453409v2>

Submitted on 28 Nov 2021

HAL is a multi-disciplinary open access archive for the deposit and dissemination of scientific research documents, whether they are published or not. The documents may come from teaching and research institutions in France or abroad, or from public or private research centers.

L'archive ouverte pluridisciplinaire **HAL**, est destinée au dépôt et à la diffusion de documents scientifiques de niveau recherche, publiés ou non, émanant des établissements d'enseignement et de recherche français ou étrangers, des laboratoires publics ou privés.

Zero-Order Second Harmonic Generation from AlGaAs-on-Insulator Metasurfaces

Giuseppe Marino,[†] Carlo Gigli,[†] Davide Rocco,[‡] Aristide Lemaître,[§] Ivan Favero,[†] Costantino De Angelis,[‡] and Giuseppe Leo^{*,†}

[†]Matériaux et Phénomènes Quantiques, Université Paris Diderot and CNRS, 10 rue Alice Domon et Léonie Duquet, 75013 Paris, France

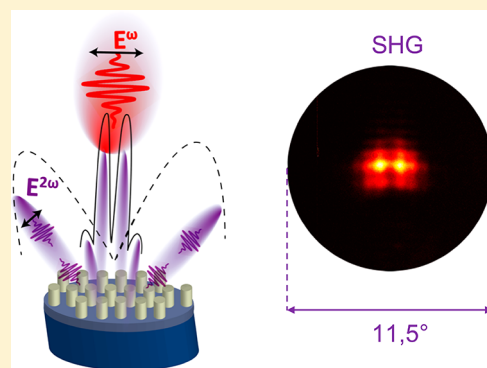
[‡]Department of Information Engineering, Università degli Studi di Brescia and INO–CNR, Via Branze 38, 25123 Brescia, Italy

[§]Centre de Nanosciences et de Nanotechnologies, CNRS - Université Paris-Saclay, Palaiseau, France

Supporting Information

ABSTRACT: All-dielectric metasurfaces consist of two-dimensional arrangements of nanoresonators and are of paramount importance for shaping polarization, phase, and amplitude of both fundamental and harmonic optical waves. To date, their reported nonlinear optical properties have been dominated by local features of the individual nanoresonators. However, collective responses typical of either Mie-resonant metamaterials or photonic crystals can potentially boost the control over such optical properties. In this work we demonstrate the generation of a second harmonic optical wave with zero-order diffraction, from a metasurface made out of AlGaAs-on-AlOx nanocylinders arranged with spatial period comparable to the pump telecom wavelength. Upon normal incidence of the pump beam, the modulation of Mie resonances via Bragg scattering at both fundamental and second harmonic frequencies enables paraxial second harmonic light generation by diffraction into the zero order, with a 50-fold increase in detected power within a solid angle of 5°. Exquisite control of a higher harmonic wavefront can be thus achieved in all-dielectric nonlinear metasurfaces, with potential applications for on-axis optical systems.

KEYWORDS: nonlinear metasurfaces, Mie resonances, nanophotonics, second-harmonic generation, all-dielectric nanophotonics, Fourier imaging



Metal-less nonlinear metasurfaces, that is to say, two-dimensional arrangements of high-refractive index nonlinear nanoresonators, have recently shown their importance for shaping polarization, phase, and amplitude of harmonic light waves.^{1–3} Since they operate in a regime where Mie-type resonances occur at both the fundamental and harmonic frequencies, such all-dielectric metasurfaces can be engineered to exhibit nonlinearly induced transparency¹ or reflection. These electromagnetic conditions are highly required for applications such as quantum imaging, where multiphoton quantum interference^{4,5} is achieved in the same nonlinear metasurface.

All-dielectric nonlinear metasurfaces have been recently studied in situations where their response is dominated by the local optical properties of the single constitutive nanoresonators, that is, for array periodicities smaller than fundamental wavelength (FW),^{1,2} but too large to enter into effective medium regime. In these cases, the incoming light was coupled to the displacement currents in the meta-atoms ($\lambda/n = \lambda_{\text{Mie}}/n \approx L$, with λ the incident FW, and n and L the meta-atom refractive index and characteristic size, respectively), while the Bragg gap was at longer wavelengths ($\lambda/n_{\text{eff}} < \lambda_{\text{Bragg}}/$

$n_{\text{eff}} = 2p$, with p being the period and n_{eff} being the effective index in the unit cell).

Today it is clear that averaged responses typical of either Mie-resonant metamaterials (which behave as a dilute system with regard to the incident light) or photonic crystals (characterized by Bragg scattering of its constituents)^{6,7} can potentially add degrees of freedom for the control of harmonic wave properties. However, while the former require $n \gg 1$ and $p \ll \lambda$,^{6,7} which is not trivial for arrays of $\chi^{(2)}$ semiconductor nanoantennas at telecom wavelengths, the more relaxed condition $p \cong \lambda$, suffices for the latter.^{8,9} In this context, Segal et al. have demonstrated the concept of nonlinear metamaterial-based photonic crystals for controlling the direction of SHG by using binary modulation of the nonlinear coefficient,¹⁰ while Löchner et al. have recently demonstrated second harmonic generation (SHG) and diffraction from a semiconductor metasurface with FW close to the material band gap.³ In both studies, for a pump at normal incidence, SHG occurred in the first order with a negligible zero order.

Received: January 21, 2019

Published: April 12, 2019

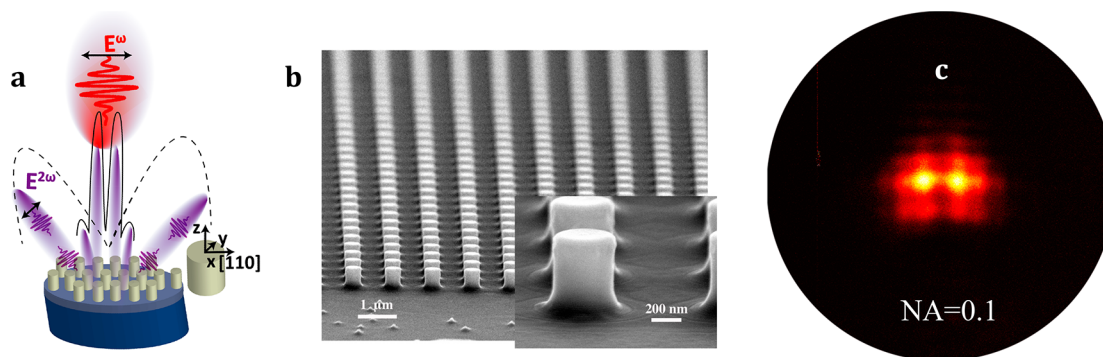


Figure 1. (a) Scheme of the AlGaAs-on-AlOx metasurface, with FW input field at normal incidence (red) and SH interference pattern (violet): the solid line represents a cut plane of the diffraction lobes at SH, while the dashed line represents a cut plane of the SHG from the isolated nanoresonator. (b) SEM image of the fabricated metasurface with $h = 400$ nm, $R = 200$ nm, and $p = 1025$ nm. (c) Measured radiation pattern of reflected SHG from AlGaAs-on-AlOx metasurface within $\text{NA} = 0.1$.

Such regime of metasurface-diffracted SHG deserves further investigation for (1) describing Mie-type resonances modulated by Bragg scattering at both FW and second harmonic (SH); and (2) the perspective of engineering both the metasurface polarizability and radiative diffraction orders via the interplay between array factor and meta-atom geometry. In particular, SHG from a metasurface-based device would greatly benefit from both pumping and emission occurring along one optical axis in the normal direction, with both FW and SH in the material transparency range.

Nonlocal modes in an array of nanoparticles have recently proved crucial for applications in sensing¹¹ and enhanced spontaneous emission.¹² At the same time, due to the confinement of FW light in confocal configurations, SHG has been established as a three-dimensional (3D) microscope imaging system with high lateral resolution.¹³ In particular, SHG in extremely confined volumes¹⁴ and with anomalous density of states¹⁵ represents a very useful tool for applications in nanomedicine¹⁶ and photocatalysis.¹⁷ In this framework, nonlocal SHG in metasurfaces has the potential to combine both the need of 3D microscopy and a large sensing area for the detection of whole biological organisms with high lateral resolution.

In this work we demonstrate zero-order SH generation and diffraction from a $\chi^{(2)}$ metasurface consisting of an array of AlGaAs nanocylinders with period comparable with the FW. Using the effective metasurface polarizability arising from the perturbation of Mie resonances via Bragg diffraction at both FW and SH, we explain the observed results and introduce a useful tool to engineer the SH radiation pattern. The choice of this semiconductor is due to the high values of its permittivity and nonlinear susceptibility.^{18–23} High-contrast AlGaAs nanoresonators with high $\chi^{(2)}$ and large bandgap have already revealed SHG efficiency up to about 10^{-6} W^{-1} with FW in the telecom range.^{21,22} This efficiency derives from the field enhancement in the nanocylinder associated with Mie resonances as well as the spatial mode coupling governed by the $\chi^{(2)}$ tensor symmetry. Although the plethora of electric and magnetic modes results in complex polarization^{22,24} and radiation patterns of the SH field,^{25–27} the latter suffers from a major limitation: a null in the forward and backward directions for normal-incidence FW illumination.²⁵

We have recently demonstrated that this issue can be solved with the use of a FW beam with an oblique incidence, thereby reshaping the SH original doughnut radiation pattern in a far-

field along the disk axis.²⁸ In that case, for an incidence angle of 45° and s-polarized light, the detected SH radiation exhibits one lobe along the vertical direction and the detected SH power within a 0.85 NA solid angle is enhanced by an order of magnitude with respect to the case of normal incidence. We have also reported another configuration, where an integrated grating redirects the SH field emitted at grazing angles from the optical antenna toward its normal.²⁹ In this case, the collected SH power within a 0.1 NA solid angle is a factor-4 higher than for the bare pillar.

Here the metasurface allows SHG within a 0.1 NA solid angle around its normal, with a 50-fold power enhancement with respect to the single nanoantenna. Correspondingly it brings the FW-to-SH cross-polarized conversion from 40% to 90%. This is achieved via a stronger coupling of the incident light with the metasurface resonances at both FW and SH with respect to the original Mie-resonances of the isolated constituents.

RESULTS AND DISCUSSION

Our metasurfaces are square arrays of $\text{Al}_{0.18}\text{Ga}_{0.82}\text{As}$ nanocylinders with radius R , height h and period p , lying upon a linear substrate with low refractive index. Both the metasurface and the substrate are linearly transparent at all the wavelengths used throughout this study. As sketched in Figure 1a, the FW input is at normal incidence and the SH is collected in reflection geometry with a pattern stemming from the overlap between Mie scattering of the single resonator and Bragg diffraction from the two-dimensional grating. Figure 1b is a scanning-electron-microscope (SEM) picture of the metasurface, with a periodic arrangement of nanocylinders of height $h = 400$ nm, radius $R = 200$ nm, and period $p = 1025$ nm. Despite the low SHG efficiency of the isolated nanoantenna in the normal direction,²⁵ thanks to the array factor, we obtain the reflected SH diffraction pattern shown in Figure 1c for a normally incident pump polarized along AlGaAs [110] crystallographic axis (see Supporting Information S1 for a schematic of the SHG setup). Here, 90% of the SHG emission is cross-polarized to the pump and presents two maxima at 1° from the vertical axis, while for a single nanoantenna, these two figures were 40° and 60° , respectively (see Supporting Information S2 for measurements of the relative intensity of zero and first order diffractions).

Design. Our metasurface is characterized by diffractive scattering of incident light at both FW and SH frequencies.

This scattering is nonlocally distributed in the metasurface plane and can interfere constructively with the Mie resonances of the isolated constituents.

In order to engineer the effective response of the metasurface, we implement the coupled-mode theory, as reported in refs 9, 30, and 31. Let us recall here that in such a model the effective electric, magnetic polarizabilities of the metasurface can be defined as $\alpha_{e,m}^{\text{meta}} = [1/\alpha_{e,m}^{\text{cyl}} - S]^{-1}$, where $\alpha_e^{\text{cyl}} = i(k^3/6\pi)^{-1}a_1$ and $\alpha_m^{\text{cyl}} = i(k^3/6\pi)^{-1}b_1$ are the electric and magnetic polarizabilities of an isolated cylinder,³² with coefficients a_1 and b_1 expressed in terms of Riccati-Bessel functions in Mie theory, and with $k = nk_0$ and k_0 the wave vectors in the medium surrounding the pillars and in vacuum (in our case $n = n_{\text{air}} = 1$). Moreover,

$$S = \sum e^{ikr} \left[\frac{(1 - ikr)(3 \cos^2 \theta - 1)}{r^3} + \frac{k^2 \sin^2 \theta}{r} \right]$$

is the array factor that embraces the coupling contribution from neighbor dipoles, with r and θ being the polar coordinates in the x - z plane of Figure 1a (here we consider only the nearest neighbors, thus, $r = p$). The effective resonances of the metasurfaces can be identified via the poles of the metasurface effective polarizability, that is, for $\text{Re}(1/\alpha_{e,m}^{\text{cyl}} - S) = 0$. At the same time, when $\text{Im}(S)$ is small or negative, a decrease of the radiative damping and, thus, an increased quality factor of Mie resonances of the isolated constituents are expected. Let us consider, for example, a metasurface with $p = 1025$ nm, $R = 200$ nm, and $h = 400$ nm. Figure 2a shows that $\text{Re}(S)$ intersects $\text{Re}(1/\alpha_e^{\text{cyl}})$ around $\lambda = 1540$ and 760 nm, and $\text{Re}(1/\alpha_m^{\text{cyl}})$ around 1570 and 770 nm. Interestingly, $\text{Im}(S)$ is negative at telecom wavelengths and slightly positive in the near infrared. In order to demonstrate the validity of the above analytical model, we report in Figure 2b the numerically calculated resonances of the metasurface. Interestingly, the latter (1) correspond to the poles of the metasurface polarizabilities when the electric and magnetic dipoles dominate the scattering (see Figure 2a,b); (2) are spectrally shifted and their Q factors double with respect to the isolated nanoresonator (compare Figure 2b with Supporting Information S3). The spectral shift is manifested for Mie dipole resonances occurring at the FW,^{8,33} for example, the electric dipole resonance of the isolated cylinder occurring at about 1275 nm (see Supporting Information S3) is shifted to 1540 nm in the metasurface case, but also at the SH, the electric dipole resonance of the isolated cylinder occurring at about 820 nm (see Supporting Information S3) is shifted to 770 nm in the metasurface case. With regard to the ability to store the energy, the metasurface increases the Q factor of the magnetic dipole at the FW from 10 (isolated cylinder) to 25, while the Q factor of the electric dipole at the SH increases from 25 (isolated cylinder) to 50. Since our description via coupled-dipoles is sufficient to predict the metasurface resonances at both FW and SH, an extension to higher-order coupled multipoles is not necessary for our scope.

The fact that the metasurface only modulates the modal structure of the isolated nanoparticle (see Supporting Information S4 for a comparison of the magnetic modes) allows to engineer the SH far field according to the following simplified model: we approximate the SH far field of the metasurface as the product between the far field of the single isolated pillar and the two-dimensional array factor including $N \times N$ cylinders, where N is a fit parameter. Figure 2c shows that

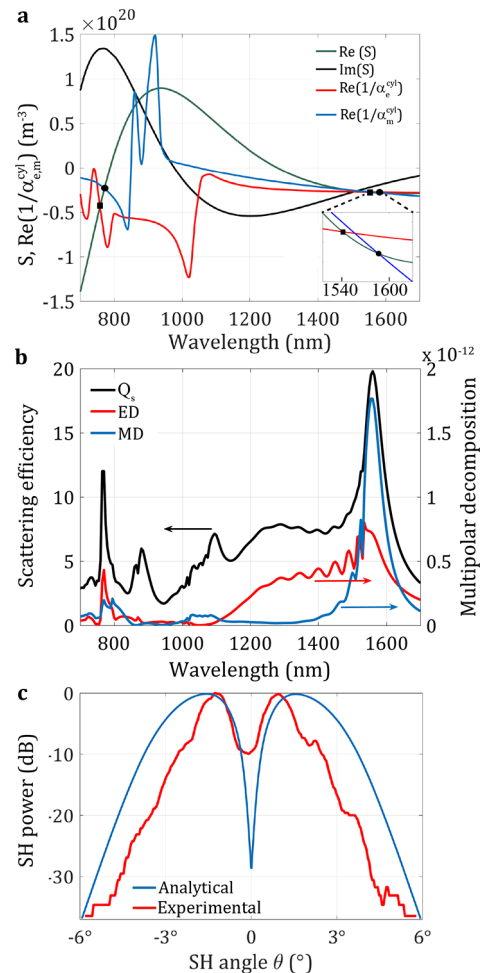


Figure 2. (a) $\text{Re}(S)$ (green line) and $\text{Im}(S)$ (black line) for a metasurface with $R = 200$ nm and $p = 1025$ nm. The red (blue) line represents the inverse of the electric (magnetic) polarizability of the single cylinder. Inset: zoom near FW. Square or circular markers represent intersections between $\text{Re}(S)$ and $\text{Re}(1/\alpha_e^{\text{cyl}})$ or $\text{Re}(1/\alpha_m^{\text{cyl}})$. (b) Scattering efficiency (Q_s) and multipolar decomposition associated with the metasurface (ED: electric dipole; MD: magnetic dipole). (c) SHG radiation pattern in the NA = 0.1 for the metasurface: analytically calculated (blue line) and experimental (red line).

the calculated SH polar plot for $N = 15$ and $p = 1025$ nm is in good agreement with the experimental one: the metasurface effectively redirects the SHG radiation into the zero-order diffraction with two maxima very close to the vertical axis ($\leq 1^\circ$). While the null at $\theta = 0$ cannot be eliminated due to the inherent symmetries of our system (zinc-blende $\chi^{(2)}$ and nanocylinder shape), this is a striking improvement with respect to the isolated nanoantenna, where far field peaks at 60° from the vertical axis. Interestingly, the choice of $N = 15$ in Figure 2c agrees well with the FW spot size (see Methods).

Parametric Study. To gain further physical insight, we measured the SHG from the AlGaAs metasurfaces by systematically varying three key parameters λ , R , and p , and we analyzed it numerically (see Methods). The SH radiation patterns measured in reflection geometry within a NA = 0.1 agree well with the calculated ones upon sweeping the pump wavelength (see Figure 3a), the meta-atom radius (see Figure 3b), and the periodicity (see Figure 3c). SHG from the metasurface with $R = 200$ nm, $h = 400$ nm, and $p = 1025$ nm

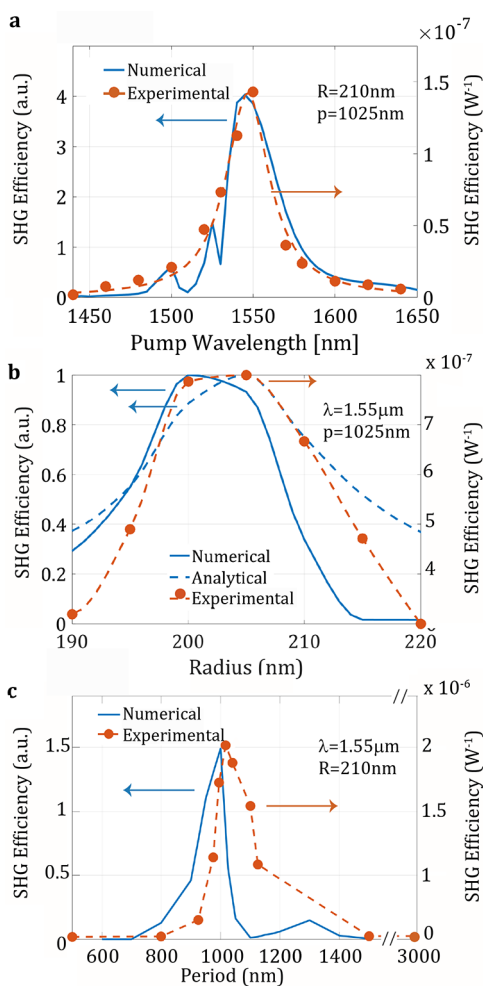


Figure 3. Zero-diffraction order SHG efficiency from metasurface in reflection geometry within 0.1 NA. Measurements (orange dots) and FEM calculations (blue solid line) vs (a) pump wavelength, for $R = 200$ nm, $h = 400$ nm, and $p = 1025$ nm; (b) nanoantenna radius, for $\lambda = 1.55 \mu\text{m}$, $p = 1025$ nm; (c) period, for $\lambda = 1.55 \mu\text{m}$ and $R = 200$ nm. In panel (b), the dashed blue line represents the analytically calculated overlap between the single nanoantenna far-field and the array factor for $N = 15$, and both blue curves are normalized to their maximum. The maximum measured efficiency is $2 \times 10^{-6} \text{ W}^{-1}$, as reported in (c). Given an input power of $1 \text{ GW}/\text{cm}^2$, SHG power in a 0.1 NA is 0.05 mW ²⁹ from the isolated cylinder and 2.6 mW from the metasurface.

has a Q factor of 50 (see Figure 3a), doubling that of the single nanoantenna with the same geometry,¹⁸ as expected from the cross section in the near-infrared region of the spectrum reported in Figure 2b.

Importantly, in Figure 3b we report the sweeping of the meta-atom radius by also using the simplified method that considers the SH far field coming from the metasurface as a multiplication between the field of the isolated pillar for the array factor (15×15) (dashed blue line of Figure 3b). This is in qualitative agreement with the method based on the Fourier transform of the SH near field coming from the metasurface (solid blue line of Figure 3b), which takes into account all possible coupling between the cylinders of the metasurface.

Finally, from Figure 3c follows that the SHG efficiency from the AlGaAs metasurface becomes negligible for periodicities smaller than the diffraction limit, where the diffraction lobe of the array factor at zero order becomes sharper and narrower,

resulting in a negligible overlap with the single nanoantenna radiation pattern. Conversely, for greater periodicities the SH modes are coupled into diffraction lobes associated with the array factor. In this case, the SHG from neighbor nanoantennas is partially diffracted toward the vertical axis, with $50\times$ enhancement with respect to the case of an isolated nanoantenna. For larger periodicity, the diffraction lobes become negligible and the efficiency within the small NA decreases, approaching the value reached for isolated nanoantennas.

CONCLUSION

We have demonstrated the engineering of the radiation pattern of all-dielectric nonlinear metasurfaces. In a square array of AlGaAs-on- AlOx nanocylinders with periodicity comparable with the wavelength of the pump light, we have measured, within a 0.1 NA, reflected cross-polarized zero-order SH diffraction outperforming by $50\times$ the SHG by an isolated nanoantenna. SH diffraction into the zero order has been modeled using the effective metasurface polarizability and the modulation of Mie-type resonances via Bragg scattering at both FW and SH. Such highly polarized SHG along the vertical axis is promising for applications like on-axis imaging and free-space optical interconnects.

METHODS

Simulations. 3D electromagnetic simulations were carried out in Comsol with finite-element-method. We modeled metasurfaces of AlGaAs nanocylinders on a substrate with refractive index $n = 1.6$, implementing Floquet boundary conditions to mimic an infinite 2D periodic structure. The permittivity dispersion of AlGaAs taken into account according to ref 34. The only nonzero elements of AlGaAs $\chi^{(2)}$ tensor are $\chi^{(2)}_{xyz} = \chi^{(2)}_{yzx} = \chi^{(2)}_{zxy}$, with $d_{14} \approx 100 \text{ pm}/\text{V}$, whose dispersion is neglected in this work. Our analysis follows three steps:²⁸ (1) we calculate the scattering from the metasurface under FW plane-wave excitation; (2) we derive SHG by taking the nonlinear polarization as a source; (3) we estimate the multipolar coefficients of FW and SH modes as in refs 32 and 35.

Fabrication. Similar to ref 21, we start from the molecular-beam epitaxy of the vertical structure: (100) GaAs (wafer)/GaAs-to- $\text{Al}_{0.98}\text{Ga}_{0.02}\text{As}$ transition layer (90 nm), $\text{Al}_{0.98}\text{Ga}_{0.02}\text{As}$ (1 μm), $\text{Al}_{0.98}\text{Ga}_{0.02}\text{As}$ -to- $\text{Al}_{0.18}\text{Ga}_{0.82}\text{As}$ transition layer (90 nm), $\text{Al}_{0.18}\text{Ga}_{0.82}\text{As}$ (400 nm). A 100 nm thick layer of high-resolution negative resist HSQ (hydrogen silsesquioxane) is spin-coated on the sample, and the nanocylinders are patterned with 20 kV electron-beam lithography. Adhesion between AlGaAs and HSQ is promoted by a thin layer of SiO_2 (10 nm) deposited by plasma-enhanced chemical vapor deposition (PECVD). The pattern is successively reported on AlGaAs with inductively coupled plasma-reactive-ion etching (ICP-RIE). The plasma, with 35 W power, aims to activate surfaces and boost the etching process. Nonselective and directional etching is performed by accelerating Ar^+ ions, present in the chamber, with a controlled pressure at 30 sccm, with 15 W RF bias. Finally, chemical selectivity toward AlGaAs is achieved, exploiting SiCl_4 gas with 3 sccm pressure. The ICP-RIE etches the nanocylinders down to the $\text{Al}_{0.98}\text{Ga}_{0.02}\text{As}$ layer. Then, the latter undergoes selective oxidation, as specified in ref 36. After oxidation, an $\text{Al}_{0.18}\text{Ga}_{0.82}\text{As}$ metasurface lies on an aluminum oxide (AlOx) substrate.

Experimental Setup. SHG from the metasurface is measured with the setup shown in [Supporting Information S1](#). The latter includes an amplitude femtosecond optical parametric amplifier with 160 fs pulse duration and repetition rate of 1 MHz. A collimated input beam with diameter $D = 3.7$ mm is focused by a 0.5 NA lens to a diffraction-limited spot with waist $w = 25 \mu\text{m}$ and peak intensity $I^{\text{FW}} \approx 0.5 \text{ GW}/\text{cm}^2$. SH signal is collected by the same lens and measured by a high-quantum efficiency CCD camera whose response was previously calibrated at 775 nm. Its emission pattern is visualized in the back focal plane by inserting a Bertrand lens. A short-pass filter at 850 nm and a long-pass filter at 700 nm are introduced in detection to remove any photoluminescence from the substrate and third harmonic emission component from the nanocylinders, respectively. On the other hand, an infinite corrected objective with NA = 0.8 was chosen to detect the first diffraction order. In this case, the pump spot size on the objective rear pupil was reduced, ensuring a collective excitation of the metasurface with a larger spot size on it. The back-focal-plane image can be found in [Supporting Information S2](#). The normalized SHG efficiency is defined as follows:

$$\eta_{\text{norm}} = \frac{\eta}{P_{\text{cyl}}^{\text{FW}}} = \frac{P_{\text{cyl}}^{\text{SH}}}{P_{\text{cyl}}^{\text{FW}^2}} (W^{-1})$$

where $P_{\text{cyl}}^{\text{SH}} = P_{\text{tot}}^{\text{SH}}/m$ (W) is the SHG power, $m = \pi w^2/p^2$ is the number of pillars lying within the laser spot size, while the power at FW impinging on the nanocylinder is $P_{\text{cyl}}^{\text{FW}} = I^{\text{FW}} \pi R^2 = (P^{\text{FW}}/\pi w^2) \pi R^2$ (W), the power of the FW beam.

■ ASSOCIATED CONTENT

Supporting Information

The Supporting Information is available free of charge on the ACS Publications website at DOI: [10.1021/acsp Photonics.9b00110](https://doi.org/10.1021/acsp Photonics.9b00110).

Schematic of the experimental setup; extended measurements; extended numerical simulations ([PDF](#))

■ AUTHOR INFORMATION

Corresponding Author

*E-mail: giuseppe.leo@univ-paris-diderot.fr.

ORCID

Giuseppe Marino: 0000-0001-8979-051X

Davide Rocco: 0000-0002-5678-0531

Giuseppe Leo: 0000-0001-6525-6734

Notes

The authors declare no competing financial interest.

■ ACKNOWLEDGMENTS

G.L. acknowledges SEAM Labex (PANAMA Project) and NOMOS project (ANR-18-CE24-0026) for financial support. G.M.'s postdoc grant was funded by PANAMA Project and EU MULTIPLY program. We all thank Aloyse Degiron et Luca Carletti for fruitful discussions.

■ REFERENCES

- (1) Wang, L.; Kruk, S. S.; Koshelev, K. L.; Kravchenko, I. I.; Luther-Davies, B.; Kivshar, Y. S. Nonlinear wavefront control with all-dielectric metasurfaces. *Nano Lett.* **2018**, *18* (6), 3978–3984.
- (2) Vabishchevich, P. P.; Liu, S.; Sinclair, M. B.; Keeler, G. A.; Peake, G. M.; Brener, I. Enhanced Second-Harmonic Generation Using

Broken Symmetry III–V Semiconductor Fano Metasurfaces. *ACS Photonics* **2018**, *5* (5), 1685–1690.

(3) Löchner, F. J.; Fedotova, A. N.; Liu, S.; Keeler, G. A.; Peake, G. M.; Saravi, S.; Shcherbakov, M. R.; Burger, S.; Fedyanin, A. A.; Brener, I.; et al. Polarization-dependent second harmonic diffraction from resonant GaAs metasurfaces. *ACS Photonics* **2018**, *5* (5), 1786–1793.

(4) Wang, K.; Titchener, J. G.; Kruk, S. S.; Xu, L.; Chung, H.-P.; Parry, M.; Kravchenko, I. I.; Chen, Y.-H.; Solntsev, A. S.; Kivshar, Y. S.; et al. Quantum metasurface for multi-photon interference and state reconstruction. *Science* **2018**, *361* (6407), 1104–1108.

(5) Stav, T.; Faerman, A.; Maguid, E.; Oren, D.; Kleiner, V.; Hasman, E.; Segev, M. Quantum entanglement of the spin and orbital angular momentum of photons using metamaterials. *Science* **2018**, *361* (6407), 1101–1104.

(6) Rybin, M. V.; Filonov, D. S.; Samusev, K. B.; Belov, P. A.; Kivshar, Y. S.; Limonov, M. F. Phase diagram for the transition from photonic crystals to dielectric metamaterials. *Nat. Commun.* **2015**, *6*, 10102.

(7) Li, S. V.; Kivshar, Y. S.; Rybin, M. V. Toward silicon-based metamaterials. *ACS Photonics* **2018**, *5*, 4751.

(8) Evlyukhin, A. B.; Reinhardt, C.; Seidel, A.; Luk'yanchuk, B. S.; Chichkov, B. N. Optical response features of Si-nanoparticle arrays. *Phys. Rev. B: Condens. Matter Mater. Phys.* **2010**, *82* (4), 045404.

(9) Auguie, B.; Barnes, W. L. Collective resonances in gold nanoparticle arrays. *Phys. Rev. Lett.* **2008**, *101* (14), 143902.

(10) Segal, N.; Keren-Zur, S.; Hendler, N.; Ellenbogen, T. Controlling light with metamaterial-based nonlinear photonic crystals. *Nat. Photonics* **2015**, *9* (3), 180.

(11) Adato, R.; Yanik, A. A.; Amsden, J. J.; Kaplan, D. L.; Omenetto, F. G.; Hong, M. K.; Erramilli, S.; Altug, H. Ultra-sensitive vibrational spectroscopy of protein monolayers with plasmonic nanoantenna arrays. *Proc. Natl. Acad. Sci. U. S. A.* **2009**, *106* (46), 19227–19232.

(12) Vecchi, G.; Giannini, V.; Rivas, J. G. Shaping the fluorescent emission by lattice resonances in plasmonic crystals of nanoantennas. *Phys. Rev. Lett.* **2009**, *102* (14), 146807.

(13) Campagnola, P. J.; Loew, L. M. Second-harmonic imaging microscopy for visualizing biomolecular arrays in cells, tissues and organisms. *Nat. Biotechnol.* **2003**, *21* (11), 1356.

(14) Kauranen, M.; Zayats, A. V. Nonlinear plasmonics. *Nat. Photonics* **2012**, *6* (11), 737.

(15) Segovia, P.; Marino, G.; Krasavin, A. V.; Olivier, N.; Wurtz, G. A.; Belov, P. A.; Ginzburg, P.; Zayats, A. V. Hyperbolic metamaterial antenna for second-harmonic generation tomography. *Opt. Express* **2015**, *23*, 30730–30738.

(16) Kachynski, A.; Pliss, A.; Kuzmin, A.; Ohulchanskyy, T.; Baev, A.; Qu, J.; Prasad, P. Photodynamic therapy by in situ nonlinear photon conversion. *Nat. Photonics* **2014**, *8* (6), 455.

(17) Clavero, C. Plasmon-induced hot-electron generation at nanoparticle/metal-oxide interfaces for photovoltaic and photocatalytic devices. *Nat. Photonics* **2014**, *8* (2), 95.

(18) Shcherbakov, M. R.; Neshev, D. N.; Hopkins, B.; Shorokhov, A. S.; Staude, I.; Melik-Gaykazyan, E. V.; Decker, M.; Ezhov, A. A.; Miroshnichenko, A. E.; Brener, I.; et al. Enhanced third-harmonic generation in silicon nanoparticles driven by magnetic response. *Nano Lett.* **2014**, *14* (11), 6488–6492.

(19) Grinblat, G.; Li, Y.; Nielsen, M. P.; Oulton, R. F.; Maier, S. A. Enhanced third harmonic generation in single germanium nanodisks excited at the anapole mode. *Nano Lett.* **2016**, *16* (7), 4635–4640.

(20) Cambiasso, J.; Grinblat, G.; Li, Y.; Rakovich, A.; Cortés, E.; Maier, S. A. Bridging the gap between dielectric nanophotonics and the visible regime with effectively lossless gallium phosphide antennas. *Nano Lett.* **2017**, *17* (2), 1219–1225.

(21) Gili, V. F.; Carletti, L.; Locatelli, A.; Rocco, D.; Finazzi, M.; Ghirardini, L.; Favero, I.; Gomez, C.; Lemaitre, A.; Celebrano, M.; De Angelis, C.; Leo, G. Monolithic AlGaAs second-harmonic nanoantennas. *Opt. Express* **2016**, *24* (14), 15965–71.

(22) Camacho-Morales, R.; Rahmani, M.; Kruk, S.; Wang, L.; Xu, L.; Smirnova, D. A.; Solntsev, A. S.; Miroshnichenko, A.; Tan, H. H.;

Karouta, F.; Naureen, S.; Vora, K.; Carletti, L.; De Angelis, C.; Jagadish, C.; Kivshar, Y. S.; Neshev, D. N. Nonlinear Generation of Vector Beams From AlGaAs Nanoantennas. *Nano Lett.* **2016**, *16* (11), 7191–7197.

(23) Liu, S.; Sinclair, M. B.; Saravi, S.; Keeler, G. A.; Yang, Y.; Reno, J.; Peake, G. M.; Setzpfandt, F.; Staude, I.; Pertsch, T.; Brener, I. Resonantly enhanced second-harmonic generation using III–V semiconductor all-dielectric metasurfaces. *Nano Lett.* **2016**, *16* (9), 5426–5432.

(24) Ghirardini, L.; Carletti, L.; Gili, V.; Pellegrini, G.; Duo, L.; Finazzi, M.; Rocco, D.; Locatelli, A.; De Angelis, C.; Favero, I.; Ravaro, M.; Leo, G.; Lemaitre, A.; Celebrano, M. Polarization properties of second-harmonic generation in AlGaAs optical nanoantennas. *Opt. Lett.* **2017**, *42* (3), 559–562.

(25) Carletti, L.; Rocco, D.; Locatelli, A.; De Angelis, C.; Gili, V.; Ravaro, M.; Favero, I.; Leo, G.; Finazzi, M.; Ghirardini, L.; Celebrano, M.; Marino, G.; Zayats, A. V. Controlling second-harmonic generation at the nanoscale with monolithic AlGaAs-on-AlOx antennas. *Nanotechnology* **2017**, *28* (11), 114005.

(26) Kruk, S. S.; Camacho-Morales, R.; Xu, L.; Rahmani, M.; Smirnova, D. A.; Wang, L.; Tan, H. H.; Jagadish, C.; Neshev, D. N.; Kivshar, Y. S. Nonlinear Optical Magnetism Revealed by Second-Harmonic Generation in Nanoantennas. *Nano Lett.* **2017**, *17* (6), 3914–3918.

(27) Guasoni, M.; Carletti, L.; Neshev, D.; De Angelis, C. Theoretical Model for Pattern Engineering of Harmonic Generation in All-Dielectric Nanoantennas. *IEEE J. Quantum Electron.* **2017**, *53* (3), 1.

(28) Carletti, L.; Marino, G.; Ghirardini, L.; Gili, V. F.; Rocco, D.; Favero, I.; Locatelli, A.; Zayats, A. V.; Celebrano, M.; Finazzi, M.; Leo, G.; De Angelis, C.; Neshev, D. N. Nonlinear Goniometry by Second-Harmonic Generation in AlGaAs Nanoantennas. *ACS Photonics* **2018**, *5* (11), 4386–4392.

(29) Ghirardini, L.; Marino, G.; Gili, V. F.; Favero, I.; Rocco, D.; Carletti, L.; Locatelli, A.; De Angelis, C.; Finazzi, M.; Celebrano, M.; Neshev, D. N.; Leo, G. Shaping the nonlinear emission pattern of a dielectric nanoantenna by integrated holographic gratings. *Nano Lett.* **2018**, *18* (11), 6750–6755.

(30) Zou, S.; Schatz, G. C. Narrow plasmonic/photonic extinction and scattering line shapes for one and two dimensional silver nanoparticle arrays. *J. Chem. Phys.* **2004**, *121* (24), 12606–12612.

(31) Markel, V. A.; Sarychev, A. K. Propagation of surface plasmons in ordered and disordered chains of metal nanospheres. *Phys. Rev. B: Condens. Matter Mater. Phys.* **2007**, *75* (8), 085426.

(32) Grahn, P.; Shevchenko, A.; Kaivola, M. Electromagnetic multipole theory for optical nanomaterials. *New J. Phys.* **2012**, *14* (9), 093033.

(33) Wang, X.; Kogos, L. C.; Paiella, R. Giant distributed optical-field enhancements from Mie-resonant lattice surface modes in dielectric metasurfaces. *OSA Continuum* **2019**, *2* (1), 32–42.

(34) Gehrsitz, S.; Reinhart, F.; Gourgon, C.; Herres, N.; Vonlanthen, A.; Sigg, H. The refractive index of Al_xGa_{1-x}As below the band gap: accurate determination and empirical modeling. *J. Appl. Phys.* **2000**, *87* (11), 7825–7837.

(35) Alaei, R.; Rockstuhl, C.; Fernandez-Corbaton, I. An electromagnetic multipole expansion beyond the long-wavelength approximation. *Opt. Commun.* **2018**, *407*, 17–21.

(36) Rahmani, M.; Leo, G.; Brener, I.; Zayats, A. V.; Maier, S. A.; De Angelis, C.; Tan, H.; Gili, V. F.; Karouta, F.; Oulton, R.; et al. Nonlinear frequency conversion in optical nanoantennas and metasurfaces: materials evolution and fabrication. *Opto-Electronic Advances* **2018**, *1* (10), 18002101.